U. S. Geological Survey Award No. 01HQGR0027

EMPIRICAL MODEL OF VERTICAL GROUND MOTIONS FOR ENGINEERING DESIGN

ABSTRACT

Principal Investigator: Igor A. Beresnev

Department of Geological and Atmospheric Sciences
Iowa State University
253 Science I
Ames, Iowa 50011-3212

Tel.: 515-294-7529
Fax: 515-294-6049
E-mail: beresnev@iastate.edu
WWW: http://www.ge-at.iastate.edu/

The current engineering approach to simulating site-specific vertical ground motions starts with rock-outcrop horizontal motions, converts them into the vertical component using an empirical *V/H* ratio for response spectra, and propagates the resulting motion through the soil column as a vertically incident *P*-wave. In the absence of data on strain-dependent soil properties in compressional deformation, strain-compatible shear-wave properties from the horizontal-component analyses are utilized. This approach makes two assumptions: (1) that the vertical motions are primarily composed of compressional waves and (2) that strain-dependent material properties in shear deformation can be extrapolated to compressional deformation. Our study deals with the empirical validation of both assumptions. First, we investigated the ratio of *SV*- to *P*-wave spectra of the vertical component of ground motions from significant recent events in California to find which wave type predominantly contributed to vertical motions, in the frequency range of 0.5 to 12.5 Hz. The results indicate that shear waves dominate the vertical motions at frequencies up to approximately 10 Hz, above which the contribution of compressional deformation is about as strong or greater. This result holds for both soil and rock sites. Second, using the data from the KiK-net borehole arrays in Japan, we estimated the nonlinearity in compressional deformation by studying *P*-wave amplification at variable amplitude levels. Frequency shifts and in some instances reduced amplification, compatible with the hysteretic softening type of nonlinearity known for shear waves, is found as the amplitude of compressional strain increases. A tentative curve of constrained-modulus reduction is also similar to the existing shear-modulus reduction curves.

The results of this study suggest that for most practical applications, vertical motions can be modeled as non-vertically propagating *SV*-waves. This could be implemented through conventional one-dimensional horizontal-component modeling using SHAKE and the application of empirical depth-dependent *V/H* correction factors to account for an inclined propagation path. At high frequencies, vertical motions may have to be modeled as near-vertically propagating *P*-waves, with strain-dependent properties

U. S. Geological Survey Award No. 01HQGR0027

EMPIRICAL MODEL OF VERTICAL GROUND MOTIONS FOR ENGINEERING DESIGN

Principal Investigator: Igor A. Beresnev

Department of Geological and Atmospheric Sciences
Iowa State University
253 Science I
Ames, Iowa 50011-3212

Tel.: 515-294-7529
Fax: 515-294-6049
E-mail: beresnev@iastate.edu
WWW: http://www.ge-at.iastate.edu/

specifically developed for compressional deformation; however, these frequencies may be of lesser importance for design applications.

BODY OF REPORT

Introduction

Proper characterization of site-specific vertical ground motions is required in a variety of engineering-design applications. The importance of this task has been emphasized by a recent observation that vertical motions can exceed horizontal motions at short periods and near-source distances (EPRI, 1993; Bozorgnia *et al.*, 1995; Silva, 1999). However, the specification of vertical motions, as compared to horizontal motions, is not nearly as well understood. The currently prevalent engineering approach starts with horizontal rock-outcrop motions and applies an empirical vertical-to-horizontal (*V/H*) ratio, established from surface records, to convert them into the vertical component. The resulting vertical motion is then propagated vertically as a compressional (*P*-) wave through a specified soil column, generally using the program SHAKE (Schnabel *et al.*, 1972; Idriss and Sun, 1992). For lack of empirical constraints, the possible *P*-wave nonlinearity is accounted for by the extrapolation of strain-dependent velocity and damping, developed for shear waves, into compressional deformation using the relationships between *P*- and *S*-wave velocities and quality factors known from linear elasticity.

As seen from above, the existing approach postulates that the vertical motions are primarily comprised of *P*-, not *SV*-, waves. This would be true for the vertical propagation; however, even a small non-zero incidence angle would make contribution from *SV*-waves rather strong, keeping in mind the large amplitudes of shear motion. The second assumption is that the nonlinearity in compressional deformation can be modeled as a scaled version of shear-wave nonlinearity, which cannot generally be true. The nonlinearity in compressional deformation may be described by a different type of constitutive law, which may or may not resemble the nonlinear rheology in shear. To develop a more rigorous model of vertical motions, one has to validate both assumptions.

These two issues are addressed in our work through the analyses of available strong-motion data. First, we consider the question of relative contribution of *P*- and *SV*-waves to the vertical component of ground motions. Second, using the recent borehole data from Japan, we study the possible manifestations of constitutive-law nonlinearity in *P*-waves. The implications of the study are discussed in the context of the improvement in the existing engineering models of vertical motions.

Contribution of *P*- and *SV*-Waves to Vertical Motions

The relative contribution of compressional and shear waves to vertical motions, as a function of frequency, can be determined by the analysis of spectra of surface motions in respective time windows. Using the strong-motion database of Pacific Engineering and Analysis, we studied the surface records of the five most significant recent earthquakes in California, at both rock and soil sites. The sites were classified according to the Geomatrix scheme: those assigned the Geomatrix categories A and B ("generic

rock and soft rock") were grouped as rock sites, and those in categories C and D ("generic soil") were grouped as soil. A total of 279 soil and 109 processed rock records from the 1983 *M* 6.4 Coalinga, 1987 *M* 6.1 Whittier Narrows, 1989 *M* 7.0 Loma Prieta, 1992 *M* 7.3 Landers, and 1994 *M* 6.7 Northridge earthquakes were utilized.

On the vertical-component records, we identified the *P*- and *SV*-wave windows and calculated the ratio of their smoothed Fourier spectra (*SV/P*) in the frequency band of 0.5 to 12.5 Hz. Since the length of the *P*-wave window, ending at *S*-wave arrival, is variable depending on the distance from the source, this length was measured first and then the identical length of the *S*-wave window was taken. To ensure a uniform processing algorithm, all traces were re-sampled to a common (lowest) sampling interval of 0.02 sec. This interval determined the high-frequency limit of 12.5 Hz for spectral-ratio calculations.

Figure 1 presents the average spectral ratios between the *SV*- and *P*-wave windows of the vertical component for (a) soil and (b) rock sites, with 95 % confidence interval of the mean and standard deviation. The ratios show that the *SV*-wave dominates the vertical motions on average at lower frequencies at both soil and rock sites. Its contribution is progressively reduced toward higher frequencies, and at frequencies of about 10 Hz, the average *P*-wave contribution is about the same. Figure 1c compares the mean ratios at soil and rock sites using a statistical *t*-test of the difference between two means. The bands around the curves are arranged in such a way that, where they do not overlap, the difference between the means is at 95 % confidence level. The rock ratio (solid lines) slightly exceeds the soil ratio (dotted lines) between approximately 0.7 and 3 Hz; at other frequencies, there is no significant difference.

We also grouped the ratios into distance (< 15 km and > 15 km) and peak-acceleration (< 0.1 *g* and > 0.4 *g*) bins, separately for rock and soil sites, to try to discriminate between the distance and nonlinearity effects, respectively. We have not found any significant differences between the distance or acceleration groups, on rock or on soil. The only difference seen was that between rock and soil similar to that in Figure 1c, in each of the distance or acceleration bins. We concluded that the site category (rock vs. soil) was the only significant factor affecting the ratios among those considered. A plausible explanation of lower ratios on soil could be the higher attenuation in *S*-waves, which reduces their contribution relative to *P*-waves. Another explanation could be the effect of near-surface refraction, which is greater at soil sites due to their higher velocity gradient, reducing the contribution of *SV*-motion (see also inset in Fig. 2).

Based on Figures 1a and b, one can separate the frequency range, in terms of a wave type controlling the vertical motions, into two intervals: below ~ 10 Hz, where *SV*-waves dominate, and above ~10 Hz, where *P*-waves are at least equally strong or may be the dominant motions. This corresponds to a cross-over period of about 0.1 sec, at which the nature of vertical motions changes.

Note that, even if the *P*-waves dominate the high frequencies, this may not be seen as a clear decrease in the *SV/P* ratio below unity. One should keep in mind that, unlike the *P*-wave window that is almost entirely composed of *P*-waves, the *SV*-wave window is a superposition of *SV*-waves over a tail of *P*-waves. If the distance from the source is sufficiently short, there will be significant *P*-wave energy extending into the *SV*-wave window. At the frequencies where *P*-waves dominate, one then will essentially divide the *P*-wave spectrum by the *P*-wave spectrum, obtaining values close to one. The

lower values can only be expected at longer distances, where only an insignificant portion of *P*-wave energy overlaps with *SV*-waves. This shows that one can only infer from the value of *SV/P* ratio close to unity that the *P*-wave is at least as strong as the *SV*-wave, whereas in reality it may be the dominant motion. The fact that *P*-waves may dominate the frequencies above ~ 10 Hz is supported by the data in Figure 2 (see following discussion).

Darragh *et al.* (1999) studied the depth variation in the response-spectral ratio between the vertical and horizontal (*V/H*) components of ground motions using the data from ten vertical arrays in California, Japan, and Taiwan. The data were grouped into six depth bins, and the average ratio was calculated for each of them. Figure 2 presents the average ratios, normalized by that at the surface. The ratios outline two distinct frequency bands where the depth behavior is different. At short periods, the ratios at depth are systematically smaller than those at the surface, whereas at long periods they are larger. The cross-over period is between 0.1 and 0.2 sec, coinciding with the above frequency separating the *SV*- and *P*-wave contributions. The frequency-dependent depth behavior, found by Darragh *et al.* (1999), then finds explanation in the corresponding change in the wave type controlling the vertical component. As the inset in Figure 2 schematically demonstrates, the *P*-wave contribution increases and *SV*-wave contribution decreases as the wave path bends toward the surface. At frequencies where *SV*-waves dominate (longer periods), one will then find the vertical component increasing with depth, while at those where *P*-waves dominate (short periods) there will be the opposite pattern. These patterns are seen to the right and to the left of the period of about 0.1 sec in Figure 2, respectively; this transitional period is marked by a vertical line at the top of Figure 2. Note that the horizontal component, dominated by *SH*-waves, will remain unaffected. Our data, showing the decreasing effect of *SV*-waves on vertical motions as frequency increases, are thus consistent with the observed depth dependence of *V/H* ratios.

Nonlinearity in Compressional Deformation

Data Used

We analyzed nonlinearity in compressional deformation by studying the near-surface amplification of *P*-waves, as a function of amplitude, using the data from the KiK-net digital borehole accelerograph arrays in Japan (http://www.kik.bosai.go.jp/). From the KiK-net online database, we selected the boreholes where the recordings of both "weak" and "strong" motions were available. The "weak" events were those whose whole-trace peak acceleration was below 0.1 *g* on all components, while the "strong" events were those whose peak acceleration in the *P*-wave window exceeded 0.1 *g* on at least one vertical component. Four boreholes were identified (OKYH09, SMNH01, SMNH02, and TTRH02). Each borehole penetrated a soil layer and ended in rock, with the exception of SMNH02, which was entirely penetrated through rock (granite). Figure 3 shows the lithology of these boreholes arranged in alphabetical order. All boreholes have two instruments: one at the surface and one at the depth of 103 m (OKYH09, TTRH02) or 104 m (SMNH01, SMNH02). All bottom instruments are in rock. Table 1 lists the parameters of all events recorded by the boreholes; the events are arranged in the

order of increasing surface PGA (peak ground acceleration) (fourth column). For convenience, the events that did not fall under the "weak" category are grouped as "strong" in Table 1, although some of them did not develop peak acceleration in the *P*-wave window exceeding 0.1 *g*. These "intermediate" events will be used for control purposes, as explained below. For the same purpose, an additional borehole (NARH01) was included.

The locations of events and boreholes are shown in Figure 4. Most of them are clustered in a limited area in the center of the expanded map. The stars, indicating earthquake epicenters, overlap, showing that the events came from a common source area. All four boreholes recorded the Tottori earthquake, the strongest *M* 7.1 event that occurred on October 6, 2000, creating a surface PGA approaching 1 *g*.

Method and Results

The idea of the method of nonlinearity analysis is to compare the near-surface amplification, calculated from the records of surface and downhole instruments, between the weak and strong motions. The amplification function is controlled by wave velocity and damping in soil, which in nonlinear soil become amplitude-dependent; the difference in the location of resonance peaks and the value of amplification between the weak and strong motions will thus indicate nonlinearity (e.g., EPRI, 1993; Beresnev and Wen, 1996).

The method of amplification-function calculation is similar to that used by Beresnev and Wen (1995). On baseline-corrected vertical-component records, we identified the *P*-wave window, cosine-tapered it, calculated the smoothed Fourier spectrum, and divided the surface spectrum by the downhole spectrum. For each borehole, we calculated the average weak-motion amplification for all weak events listed in Table 1; these average functions are plotted in Figure 5 as thin lines, with the 95 % confidence intervals of the mean (dotted lines). The boreholes are arranged in alphabetical order. Figure 5 also presents the strong-motion amplifications, separately for each of the events listed as "strong" in Table 1 (thick lines). The strong-event origin time and maximum acceleration in *P*-wave window are listed in the upper left and right corners of the plots, respectively. For each of the four boreholes, there is only one event whose *P*-wave acceleration exceeded 0.1 *g*; this is the *M* 7.1 Tottori earthquake mentioned above (*P*-wave accelerations of ~ 115, 255, 120, and 340 cm/sec^2 at OKYH09, SMNH01, SMNH02, and TTRH02, respectively). Figure 6 shows the three components of ground acceleration for this event recorded at TTRH02; this borehole recorded the strongest motions. All other events fall below the 0.1 *g* *P*-wave acceleration level and are arranged in the order of decreasing *P*-wave acceleration. They are used for control purposes, so is the borehole NARH01.

The known common manifestations of nonlinearity in *S*-waves are the shift in the resonance frequency to lower values and the reduction in amplification, as the amplitude of motions increases, characteristic of the hysteretic "softening" type of nonlinearity (Silva, 1986; Beresnev and Wen, 1996; Field *et al.*, 1997; Dimitriu *et al.*, 2000). Figure 6 shows the *S*-wave nonlinearity clearly as a nonlinear response of the sand and gravel layer at TTRH02 borehole to the shear wave; the period of shear motion becomes visibly longer at horizontal components of the surface instrument compared to those in granite at

depth. The significant decrease in the resonance frequency can be directly shown if the shear-wave uphole/downhole spectral ratio is compared to that in weak events (not reproduced here).

Patterns, similar to *S*-wave nonlinearity, can be seen in *P*-wave amplification for the Tottori event at boreholes OKYH09 (Fig. 5b), SMNH01 (Fig. 5c), and TTRH02 (Fig. 5h), or the boreholes that penetrated the soft soil material. A frequency shift of the main weak-motion amplification peak of up to 0.7 Hz (at OKYH09) is observed; the reduction in amplification is also seen in Figures 5b and 5h. The magnitude of the frequency shift is comparable to that typically observed for shear waves (e.g., Beresnev *et al.*, 1998). The only borehole that does not exhibit a visible shift for the same event is SMNH02 (Fig. 5g); however, this is the borehole drilled entirely in hard rock.

The amplifications measured at boreholes SMNH01 and TTRH02 for the "intermediate" events (overall peak acceleration exceeding 0.1 *g* but *P*-wave acceleration below 0.1 *g*) are plotted in Figures 5d-f and 5i-l. The downward shift in resonance frequency disappears for these events, supporting the argument that the shift observed for the strong event is caused by *P*-wave nonlinearity. Finally, Figure 5a provides one more control example. The thick line corresponds to another intermediate event, recorded by borehole NARH01, with peak *P*-wave acceleration of 49 cm/sec^2. The borehole was drilled in soft slate material. The amplification function for this event virtually coincides with the average weak-motion amplification. We conclude that the shifts in the resonance frequency, seen in Figure 5 for the strongest (Tottori) event, are caused by the nonlinear soil response to compressional deformation. The nonlinearity in *P*-waves is observable at the acceleration levels roughly exceeding 0.1 *g*. The manifestation of the effect is similar to that typically observed in *S*-waves.

Beresnev and Wen (1995) came to a different conclusion when performing similar analyses for a strong event recorded by the Lotung borehole array in Taiwan drilled in soft sediments. There was no detectable difference between the location of the resonance peak nor the level of amplification between the "weak" and "strong" motions, calculated for the events selected according to the same criterion. The peak *P*-wave acceleration was 109 cm/sec^2, which is significantly lower that those observed in Figures 5c and 5h and slightly lower than that in Figure 5b. The KiK-net data provide evidence supporting the nonlinear response of soil to compressional deformation; to further constrain the characteristics of *P*-wave nonlinearity, similar analyses should be performed as more data are collected.

Reasonable caution should be exercised in ascertaining that the main weak-motion resonance peaks, observed as shifting in Figures 5b (OKYH09), 5c (SMNH01), and 5h (TTRH02), are associated with the *P*-, not *S*-, waves; some presence of *S*-wave energy in the *P*-wave window cannot be ruled out for extended sources. To look into this issue, we calculated the theoretical spectral ratios between the surface and bottom instruments for the above boreholes of interest. The ratios were calculated using the reflection/transmission matrix method of Kennett and Kerry (1979), assuming a *P*-wave incident from below. The borehole *P*- and *S*-wave velocity profiles, used for the theoretical-response calculations, are available from the KiK-net WWW site (see above) and are reproduced in Figure 7. Densities (ρ) were not reported; they were generated using the empirical Gardner's rule: $\rho = aV_P^{1/4}$, where V_P is the *P*-wave velocity in m/sec, density is in g/cm^3, and $a = 0.31$ (Sheriff and Geldart, 1995, equation 5.15). Also, the

absolute value of theoretical ratios will depend on the quality factors Q in the profile, which were not measured. However, the choice of Q is unimportant for the purposes of this analysis, since we are only interested in the frequency of the peaks and not their absolute value. We thus arbitrarily assumed Q to be 100 and 1000 in the soil and rock layers, respectively. The theoretical spectral ratios for the vertical component are presented in Figure 8 for two incidence angles, 0° and 10°.

Figure 8 shows that the main weak-motion resonance peaks observed in Figure 5 are the fundamental (lowest) resonances of the *P*-wave, with an almost exact match between the observed and theoretically calculated frequencies. The variation in the angle of incidence leaves the ratios almost unaffected. This calculation supports the conclusion that we deal with the resonance in *P*-wave motions and that the shift is attributed to *P*-wave nonlinearity.

Using the observed resonance-frequency shifts (Δf), the corresponding changes in the elastic moduli controlling *P*-wave velocity can be estimated. Using $V_P = (M/\rho)^{1/2}$, where $M \equiv K + (4/3)\mu$, and K and μ are the bulk and shear moduli, respectively, the ratio between the strong-motion modulus (M_s) and weak-motion modulus (M_w) can be written as

$$M_s/M_w = (1 - \Delta f / f_w)^2, \qquad (1)$$

where f_w is the weak-motion resonance frequency (Beresnev *et al.*, 1998, equation 2). The modulus M is the "constrained modulus" in geotechnical terminology. The surface compressional strain can be estimated from vertical acceleration records, as also described by Beresnev *et al.* (1998). We applied this approach to the frequency shifts observed in Figs. 5b, 5c, and 5h. We also assumed that nonlinearity is non-detectable (modulus ratio of 1) in Figs. 5a, 5d, and 5i, as the level of acceleration drops. The results of these calculations are shown in Figure 9 (solid circles) as the chart of constrained-modulus ratio (M_s/M_w) in the surficial layer as a function of strain amplitude at the surface. The data exhibit considerable scatter but illustrate the order of magnitude of the modulus-reduction effect. The compressional-strain level marking the transition between the linear and nonlinear responses (~10^{-3} percent, Figure 9) matches closely that for shear waves, as seen from the EPRI (1993) shear-modulus reduction guidelines for sand also reproduced in Figure 9 (open circles). The EPRI data are the average over the depth range of 0-15 m (0-50 ft). It is not clear whether the strain dependence of the constrained modulus is primarily caused by the respective change in the shear modulus (μ) or bulk modulus (K), since the evaluation of M based on resonance frequency (controlled by *P*-wave velocity) does not allow separation of these contributions. However, it seems unlikely that compressional strain could significantly alter the shear modulus, so one could hypothesize that the reduction in M is primarily caused by the reduction in bulk modulus K, while μ remains approximately constant. However, this is purely speculative at this time. The question of how much the bulk modulus K varies with strain thus remains open. Also, more data clearly are needed to better constrain the modulus reduction curve, such as in Figure 9, to the more specific shape similar to that developed for shear modulus. The data shown should be considered preliminary and illustrating the order of magnitude of the effect.

It is clear that the degree of nonlinearity in compressional waves will depend significantly on the presence of fluids in porous space, and will likely be limited to the sections above water table. The *P*-wave velocity profiles shown in Figure 7 indicate that their top portions were above water table at the time of measurements (velocities much lower than the speed of sound in water) and probably remained so during the Tottori earthquake, which might have made the detection of nonlinear response possible.

Nonlinearity in the propagation of *P*-waves in earth materials is not something entirely new. The hysteretic softening nonlinearity has been reported for *P*-waves with strain as low as 10^{-8} propagating in dry sandstone (Guyer and Johnson, 1999). From those and the present findings, compressional-wave nonlinearity seems to be of the same type known for shear waves. It has nevertheless not been observed before in strong ground motions with the potential for engineering use.

Conclusions

The results of this study suggest how the existing procedures for engineering development of site-specific vertical motions could be modified. Contrary to the current view, we have found that shear (*SV*-) waves dominate vertical motions at frequencies up to approximately 10 Hz. For practical purposes, the design motions should thus be modeled as near-vertically propagating *SV*-, not *P*-, waves, traversing the specified soil column. At frequencies below 10 Hz, which cover a broad range of engineering applications, the equivalent-linear analyses based on SHAKE could first be applied to synthesize the vertically propagating *SH*-component. To convert the simulated *SH*-motion into *SV*-motion at a desired depth, and thus account for the inclined path of realistic *SV*-wave propagation, the empirical correction factors, such as developed by Darragh *et al.* (1999) (Fig. 2) could be used. The strain-dependent soil properties, serving as input to SHAKE, will be the same assumed for shear waves.

The simulation algorithm may become different if frequencies higher than ~ 10 Hz are of interest. As Figure 1 shows, *P*-waves may become a significant contributor to the vertical motions at high frequencies. In this case, vertical motions could still be modeled with SHAKE but as vertically propagating *P*-waves with strain-dependent soil properties specific for *P*-waves. Corrections for non-vertical incidence, similar to the above *V/H* factors but specific for *P*-waves, would have to be applied, which have not been developed yet.

Future studies should also address the two outstanding issues existing in the outlined approach. First, they should investigate the *SV*- to *P*-wave spectral ratios on vertical components, as in Figure 1, at frequencies above 12.5 Hz, to find if the trend toward exceedance of *P*-wave energy continues into higher frequencies. Second, *P*-wave strain-dependent soil properties (such as in Figure 9), including damping, should be developed independently of shear waves. There are indications that they may be similar to those for shear waves. It might also be true that even at higher frequencies, vertical motions could still be modeled with sufficient accuracy as near vertically propagating *SV*-waves, which makes simulations at all frequencies straightforward to implement.

Acknowledgments

This work was supported by U. S. Geological Survey - National Earthquake Hazards Reduction Program (NEHRP) under contract No. 01HQGR0027. The use of the data from KiK-net network in Japan, available through the Internet, is greatly appreciated. We are grateful to N. Gregor for stimulating discussions. The reflection/transmission FORTRAN code written by J.-C. Gariel was used. Figure 4 was prepared with Generic Mapping Tools (GMT) (Wessel and Smith, 1998).

References

Beresnev, I. A. and K.-L. Wen (1996). Nonlinear soil response - a reality? (A review), *Bull. Seism. Soc. Am.* **86**, 1964-1978.

Beresnev, I. A. and K.-L. Wen (1995). *P*-wave amplification by near-surface deposits at different excitation levels, *Bull. Seism. Soc. Am.* **85**, 1490-1494.

Beresnev, I. A., Field, E. H., Van Den Abeele, K., and Johnson, P. A. (1998). Magnitude of nonlinear sediment response in Los Angeles basin during the 1994 Northridge, California, earthquake, *Bull. Seism. Soc. Am.* **88**, 1079-1084.

Bozorgnia, Y., M. Niazi, and K. W. Campbell (1995). Characteristics of free-field vertical ground motion during the Northridge earthquake, *Earthquake Spectra* **11**, 515-525.

Darragh, B., W. Silva, and N. Gregor (1999). Bay Bridge downhole array analyses, Rept. submitted to Earth Mechanics, Inc., Fountain Valley, California.

Dimitriu, P., N. Theodulidis, and P.-Y. Bard (2000). Evidence of nonlinear site response in HVSR from SMART1 (Taiwan) data, *Soil Dyn. Earthquake Eng.* **20**, 155-165.

Electric Power Research Institute (EPRI) (1993). Guidelines for determining design basis ground motions, Volume 1 – Method and guidelines for estimating earthquake ground motion in Eastern North America, Rept. EPRI TR-102293, Palo Alto, California.

Field, E. H., P. A. Johnson, I. A. Beresnev, and Y. Zeng (1997). Nonlinear ground-motion amplification by sediments during the 1994 Northridge earthquake, *Nature* **390**, 599-602.

Guyer, R. A. and P. A. Johnson (1999). Nonlinear mesoscopic elasticity: evidence for a new class of materials, *Physics Today* (April), 30-36.

Idriss, I. M. and J. I Sun (1992). User's manual for SHAKE91, a computer program for conducting equivalent linear seismic response analyses of horizontally layered soil deposits, Center for Geotechnical Modeling, Department of Civil and Environmental Engineering, University of California, Davis.

Kennett, B. L. N. and N. J. Kerry (1979). Seismic waves in a stratified half space, *Geophys. J. R. Astr. Soc.* **57**, 557-583.

Schnabel, P. B., J. Lysmer, and H. B. Seed (1972). SHAKE: A computer program for earthquake response analysis of horizontally layered sites, Rept. UCB/EERC 72/12, Earthquake Engineering Research Center, University of California, Berkeley.

Sheriff, R. E. and L. P. Geldart (1995). *Exploration Seismology*, 2nd ed., Cambridge University Press, 592 pp.

Silva, W. J. (1986). Soil response to earthquake ground motion, Rept. prepared for Electric Power Research Institute, EPRI Research Project RP 2556-07.

Silva, W. J. (1999). Characteristics of vertical strong ground motions for applications to engineering design, in *Proc. of the FHWA/NCEER Workshop on the National Rep. of Seismic Ground Motion for New and Existing Highway Facilities,* Technical Rept. NCEER-97-0010.

Wessel, P. and W. H. F. Smith (1998). New, improved version of Generic Mapping Tools released, *EOS* **79**, 579.

Figure Captions

Figure 1. Average ratios of Fourier spectra of *SV*- and *P*-wave windows on vertical component of ground motions: (a) California soil sites, (b) California rock sites, (c) statistical test of difference between soil and rock means.

Figure 2. Average *V/H* response-spectral ratios (5 % damping) for six depth ranges, combined from observations at ten borehole accelerograph arrays. The ratios are normalized by the surface ratio, which plots as the solid line at unity (after Darragh *et al.*, 1999). The inset explains how the contribution of particle motions in *SV*- and *P*-waves changes as propagation path bends toward the surface. The vertical line marks the transitional frequency at which the wave type primarily contributing to the vertical motions changes.

Figure 3. Lithology of KiK-net boreholes used in *P*-wave nonlinearity analyses. Source: KiK-net WWW site (http://www.kik.bosai.go.jp/).

Figure 4. (Left) Map of Japan with the area (boxed) in which the selected events and boreholes are located. (Right) Blown-up view of the boxed area.

Figure 5. Empirical site amplification functions at KiK-net borehole sites. The boreholes are arranged in alphabetical order. The thin line shows the average weak-motion amplification for each borehole; the dotted line is the 95 % confidence interval of the mean. The thick line is the amplification function for a strong event. The origin time of the strong event and its peak acceleration in *P*-wave window on the vertical component (in cm/sec^2) are indicated in the upper left and right corners, respectively. For each borehole, the strong events are arranged in the order of decreasing *P*-wave acceleration; the weak-motion amplification function is the same.

Figure 6. Three components of acceleration recorded by borehole TTRH02 during the *M* 7.1 Tottori earthquake at the surface (left) and 103 m (right). The whole-trace maximum acceleration is listed to the left of the traces.

Figure 7. *P*- and *S*-wave velocity structures for the three KiK-net boreholes.

Figure 8. Theoretical *P*-wave spectral ratios between the surface and downhole instruments for the velocity profiles shown in Figure 7.

Figure 9. Constrained-modulus reduction effect (solid circles) from *P*-wave amplification data. The EPRI (1993) guidelines for shear-modulus reduction in sand are shown for reference (open circles).

Table 1

Selected KiK-Net Events

Event Date and Time	Magnitude*	Epicentral Distance (km)	Maximum Surface PGA (*g*)
	NARH01		
	Weak Events		
2000 0602 1506	4.3	24	.012
2000 0428 1142	4.5	8	.022
1998 1111 0027	3.7	23	.029
	Strong Event		
1999 0821 0533	5.5	15	.161
	OKYH09		
	Weak Events		
2000 1008 0621	3.7	26	.003
2000 1007 0824	3.7	26	.010
2000 1030 1558	3.7	26	.011
2000 1006 1625	3.6	17	.012
2000 1006 2257	4.4	26	.015
2000 1105 0300	4.0	2.6	.021
2000 1006 1654	4.0	26	.023
2000 1007 0459	4.9	29	.032
2000 1017 2217	4.6	26	.059
	Strong Event		
2000 1006 1330	7.1	29	.289
	SMNH01		
	Weak Events		
2000 1104 0429	3.5	12	.004
2000 1220 1004	3.7	12	.006
2001 0122 1320	3.8	12	.007
2000 1129 2135	2.9	13	.008
2000 1104 0715	3.9	12	.013
2001 0116 1806	3.8	16	.013
2000 1030 1558	3.7	16	.015
2000 1113 1832	3.9	12	.015
2000 1219 0618	4.3	12	.018
2000 1018 0805	3.9	12	.027
2000 1012 1707	3.9	3	.029
2000 1104 1048	3.8	12	.038
2000 1103 1633	4.7	27	.039
2000 1013 1044	3.6	13	.040
2000 1014 0336	3.7	3	.042
2000 1207 2309	4.5	12	.050
2000 1017 2217	4.6	16	.051
2000 1006 1957	4.0	3	.060
2000 1018 1422	3.8	3	.064
2000 1018 0000	3.4	3	.068
2000 0717 0800	4.6	17	.072
2000 1007 0622	4.2	3	.087

2000 1018 2339	4.0		11	.090
2000 1010 0226	3.5		3	.092
2000 1007 0749	4.3		13	.093
2000 1006 2313	4.4		3	.096
		Strong Events		
2000 1017 2210	3.7		3	.108
2000 1007 1832	4.2		3	.159
2000 1007 0459	4.9		13	.259
2000 1006 1330	7.1		13	.735
		SMNH02		
		Weak Events		
2000 1007 0638	4.4		28	.008
2000 1007 0749	4.3		30	.016
2000 1007 1203	4.5		28	.018
2000 1006 2129	4.1		21	.024
2000 1006 1957	4.0		21	.025
2000 1006 1638	3.5		30	.027
2000 1007 0459	4.9		30	.039
2000 1006 2313	4.4		21	.046
2000 1010 2158	4.6		28	.050
		Strong Event		
2000 1006 1330	7.1		30	.575
		TTRH02		
		Weak Events		
2000 1019 0803	3.8		21	.010
2000 1103 1653	3.7		21	.010
2000 1129 2135	2.9		8	.011
2000 1104 1048	3.8		21	.012
2000 1220 1004	3.7		21	.015
2001 0122 1320	3.8		21	.015
2000 1104 0715	3.9		21	.017
2000 1018 2339	4.0		9	.022
2000 1113 1832	3.9		21	.023
2000 1030 1558	3.7		3	.042
2000 1219 0618	4.3		21	.042
2000 1207 2309	4.5		21	.064
2000 1013 1044	3.6		8	.082
		Strong Events		
2001 0116 1806	3.8		3	.103
2000 1105 0300	4.0		3	.128
2000 1009 0114	3.5		3	.135
2000 1017 2217	4.6		3	.163
2000 1006 1330	7.1		8	.946

* Definition of magnitude not found on KiK-net WWW site. Apparently, this is the JMA (Japan Meteorological Agency) magnitude.

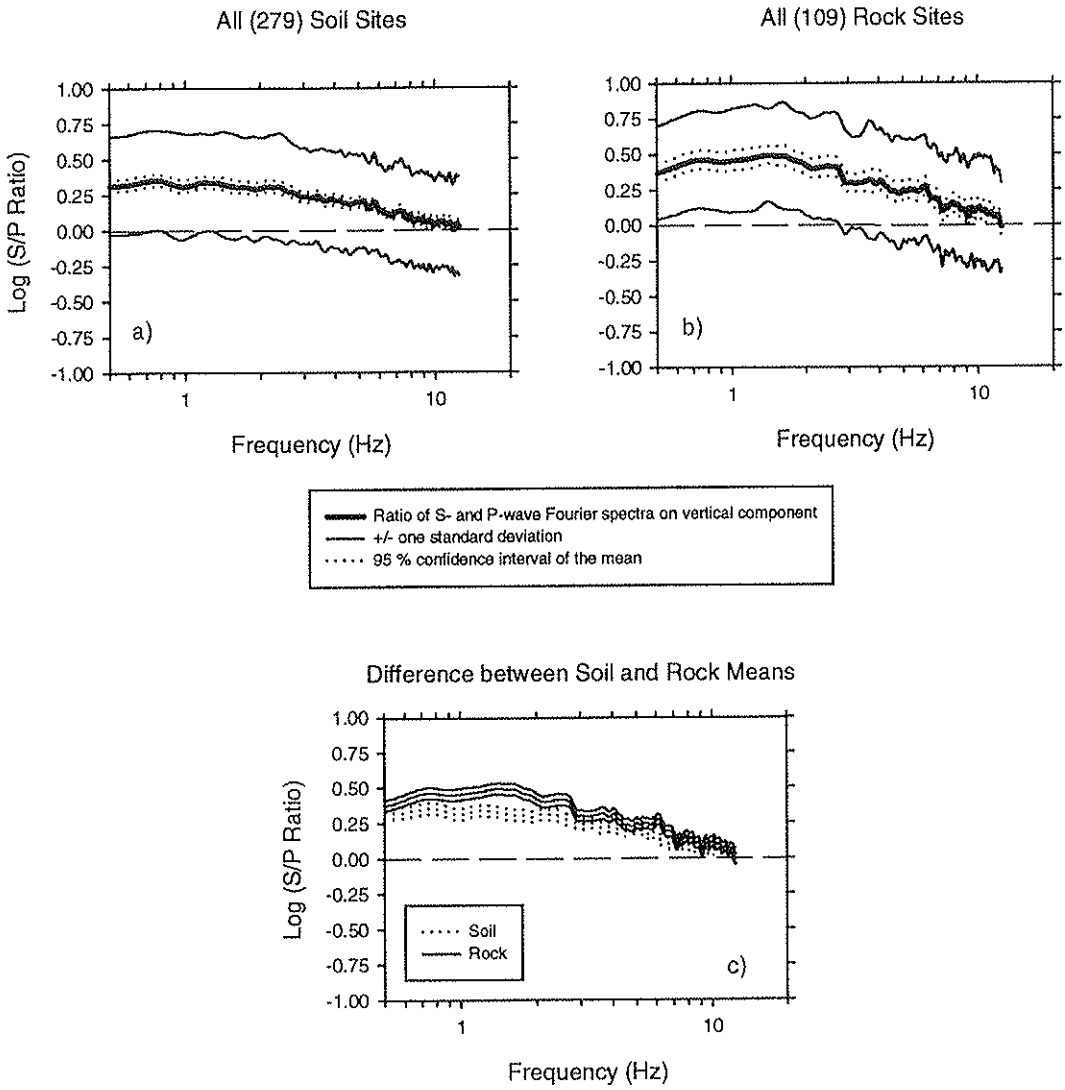

Figure 1. Average ratios of Fourier spectra of *SV*- and *P*-wave windows on vertical component of ground motions: (a) California soil sites, (b) California rock sites, (c) statistical test of difference between soil and rock means.

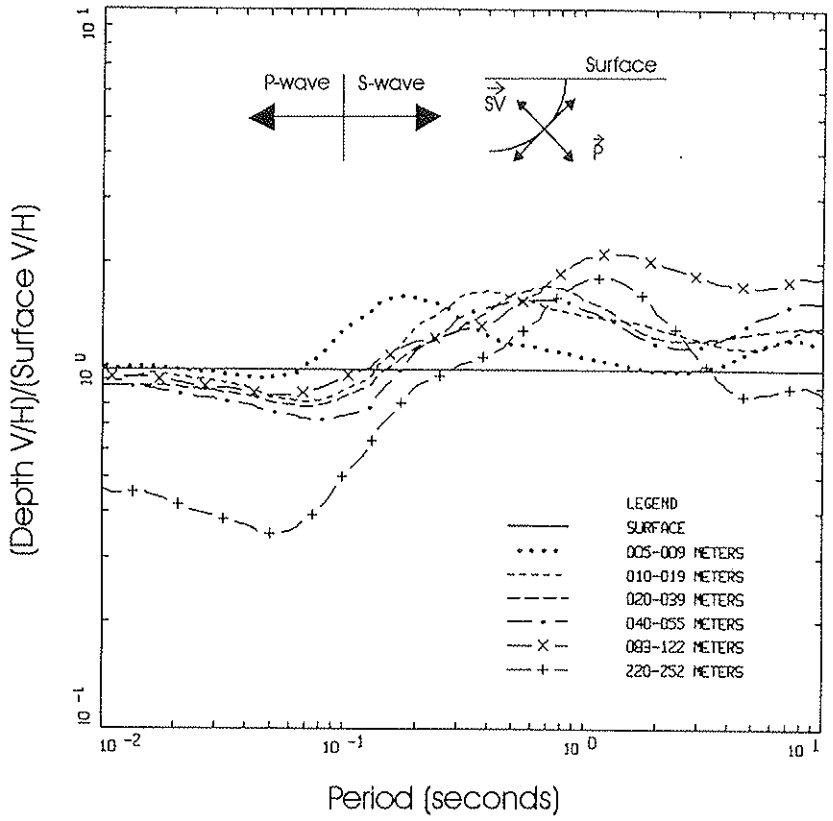

Figure 2. Average *V/H* response-spectral ratios (5 % damping) for six depth ranges, combined from observations at ten borehole accelerograph arrays. The ratios are normalized by the surface ratio, which plots as the solid line at unity (after Darragh *et al.*, 1999). The inset explains how the contribution of particle motions in *SV*- and *P*-waves changes as propagation path bends toward the surface. The vertical line marks the transitional frequency at which the wave type primarily contributing to the vertical motions changes.

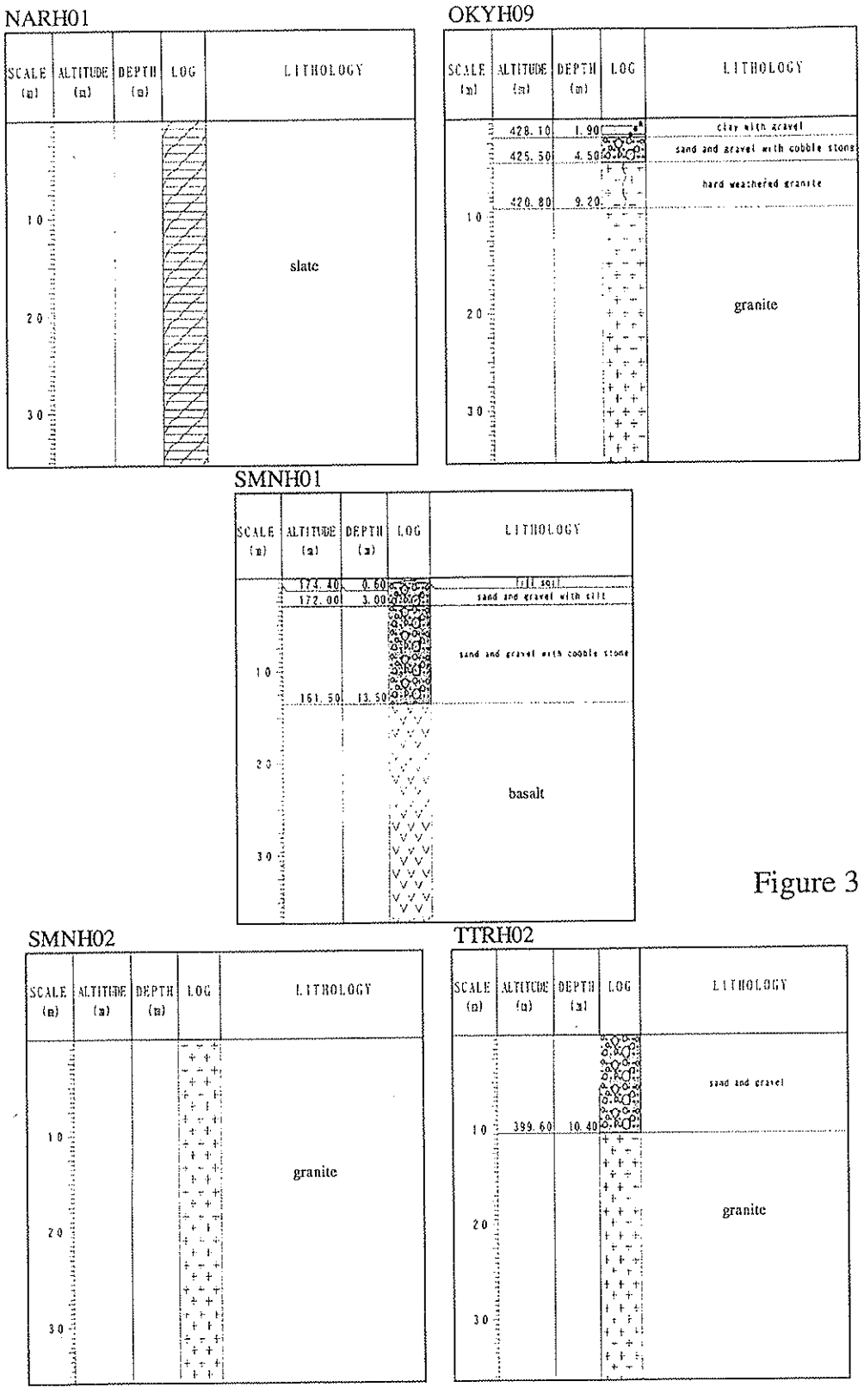
NARH01
SCALE (m)
ALTITUDE (m)
DEPTH (m)
LOG
LITHOLOGY
10
20
30
slate
OKYH09
SCALE (m)
ALTITUDE (m)
DEPTH (m)
LOG
LITHOLOGY
428.10
1.90
clay with gravel
425.50
4.50
sand and gravel with cobble stone
420.80
9.20
hard weathered granite
10
20
30
granite
SMNH01
SCALE (m)
ALTITUDE (m)
DEPTH (m)
LOG
LITHOLOGY
173.40
0.60
fill soil
172.00
3.00
sand and gravel with silt
sand and gravel with cobble stone
10
161.50
13.50
20
basalt
30
SMNH02
SCALE (m)
ALTITUDE (m)
DEPTH (m)
LOG
LITHOLOGY
10
granite
20
30
TTRH02
SCALE (m)
ALTITUDE (m)
DEPTH (m)
LOG
LITHOLOGY
sand and gravel
10
399.60
10.40
granite
20
30

Figure 3

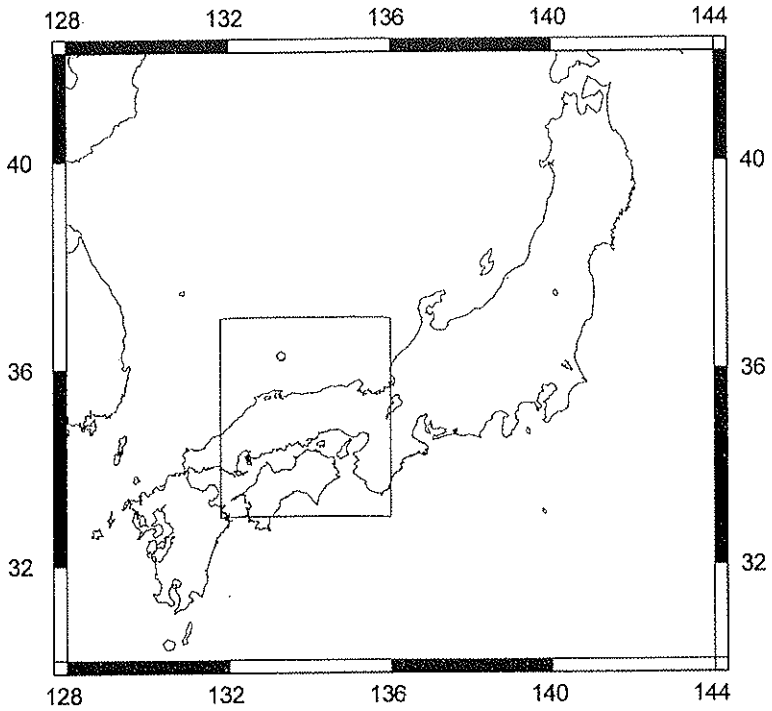
128
132
136
140
144
40
36
32

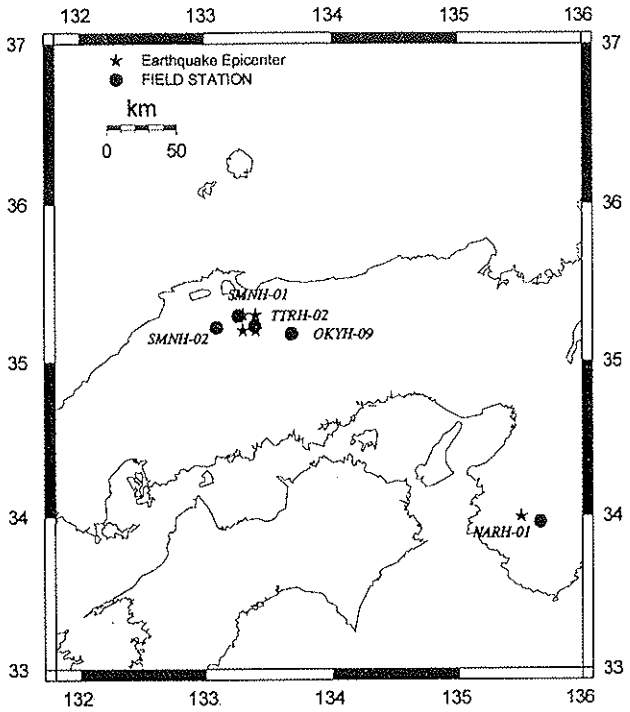
132
133
134
135
136
37
36
35
34
33
Earthquake Epicenter
FIELD STATION
km
0
50
SMNH-01
TTRH-02
SMNH-02
OKYH-09
NARH-01

F4

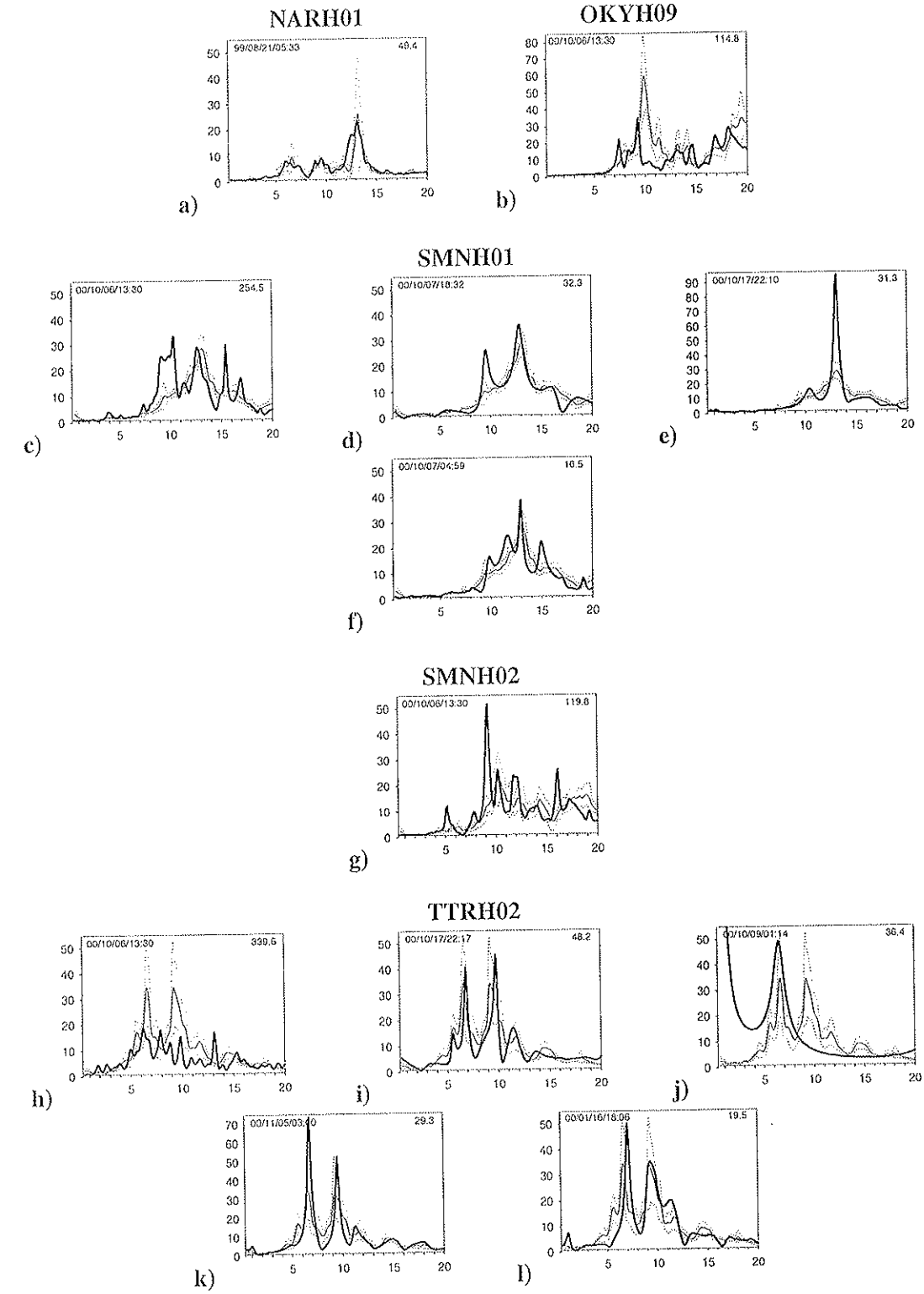
NARH01
99/08/21/05:33
40.4
a)
OKYH09
00/10/06/13:30
114.8
b)
SMNH01
00/10/06/13:30
254.5
c)
00/10/07/18:32
32.3
d)
00/10/17/22:10
31.3
e)
00/10/07/04:59
16.5
f)
SMNH02
00/10/06/13:30
119.8
g)
TTRH02
00/10/06/13:30
339.6
h)
00/10/17/22:17
48.2
i)
00/10/09/01:14
36.4
j)
00/11/05/03:40
29.3
k)
00/01/16/18:06
19.5
l)
Strong Event
Average Weak Events (<.1g)
95% Confidence Interval

Figure 5

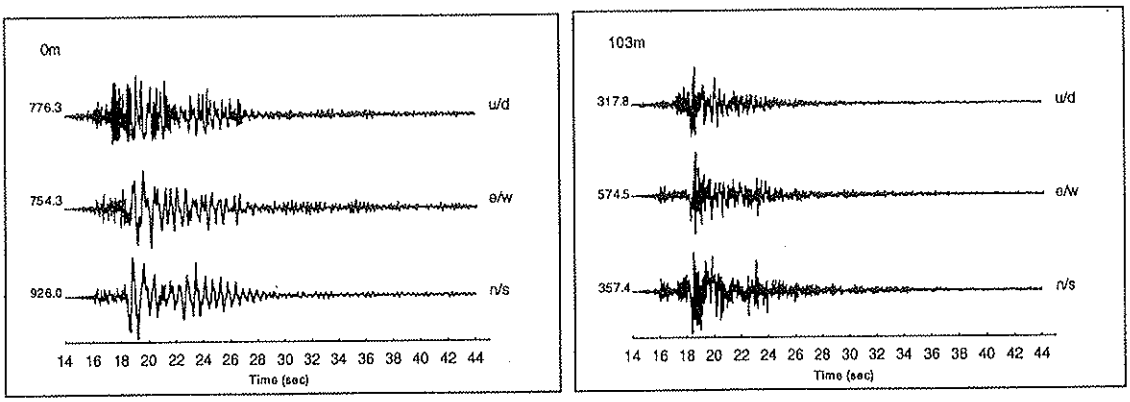

Figure 6. Three components of acceleration recorded by borehole TTRH02 during the *M* 7.1 Tottori earthquake at the surface (left) and 103 m (right). The whole-trace maximum acceleration is listed to the left of the traces.

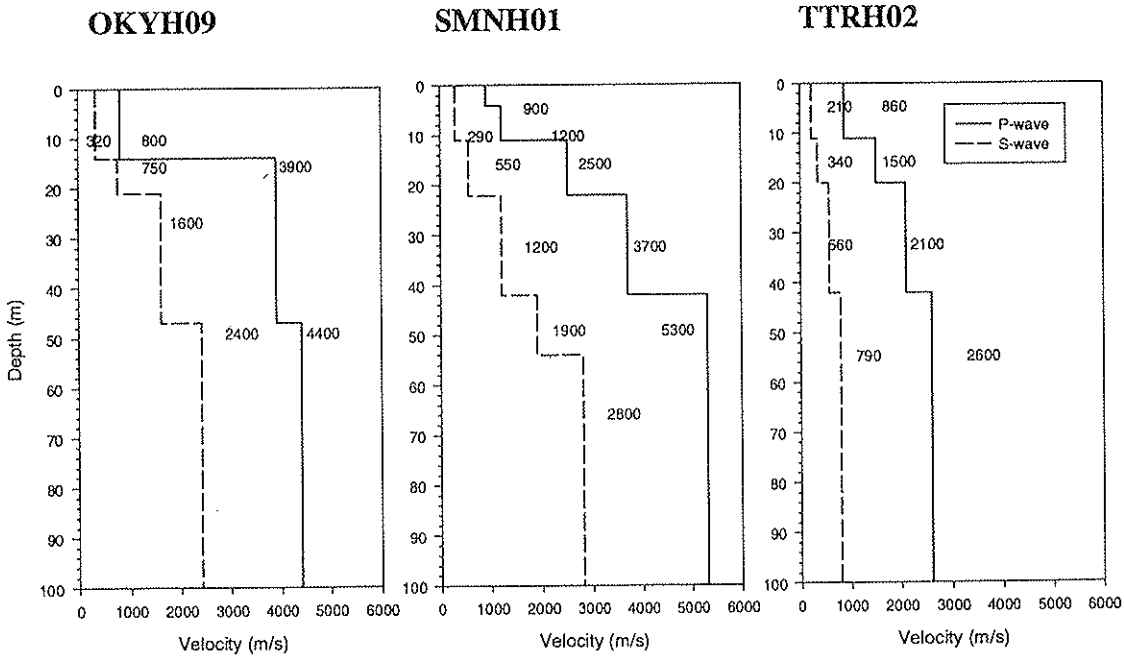

Figure 7. *P*- and *S*-wave velocity structures for the three KiK-net boreholes.

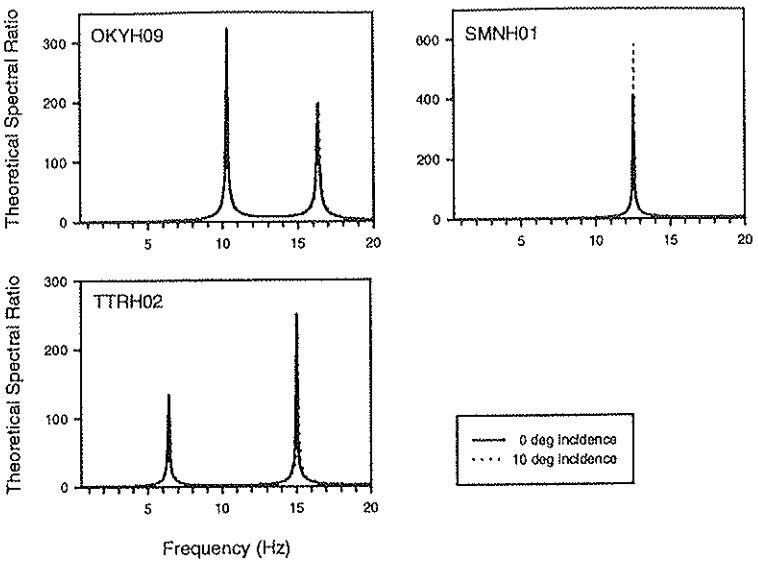

Figure 8. Theoretical *P*-wave spectral ratios between the surface and downhole instruments for the velocity profiles shown in Figure 7.

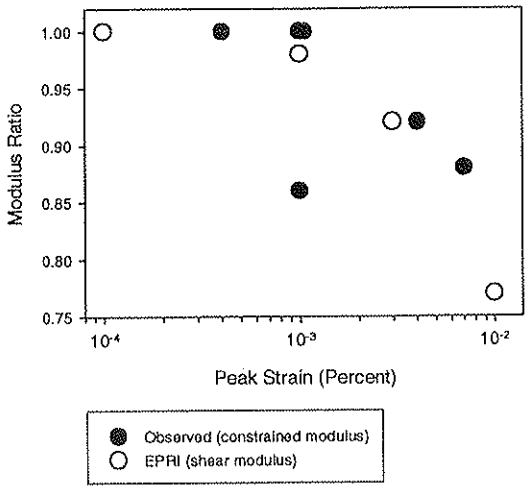

Figure 9. Constrained-modulus reduction effect (solid circles) from *P*-wave amplification data. The EPRI (1993) guidelines for shear-modulus reduction in sand are shown for reference (open circles).

BIBLIOGRAPHY

This report has also been submitted in December 2001 as a paper to the *Bulletin of the Seismological Society of America.* Title of the paper: "Properties of vertical ground motions", authors: I. A. Beresnev, A. M. Nightengale, and W. J. Silva.

Slip Behavior of Faults through Several Earthquake Cycles
Award Number 01-HQ-GR-0002

Kerry Sieh
1200 E. California Blvd.
California Institute of Technology
Mail Code 100-23
Pasadena, CA 91125
Tel: 626-395-6115
Fax: 626-564-0715
sieh@gps.caltch.edu

NEHRP Element: II
Key Words: Paleoseismology, Trench Investigation, Fault Segmentation, Quaternary Fault Behavior

Investigations Undertaken

This study is designed to document the offsets of recurrent earthquakes at a single location to see how slip varies through earthquake cycles. One of the best places to determine if a fault segment experiences similar amount of slip through time is a 100-meter section along the Carrizo segment of the San Andreas fault, just a few hundred meters southeast of Wallace Creek (Figure 1). There, small channels about a half-meter deep are cut by the simple, narrow, rectilinear trace of the San Andreas fault, three such small channels (labeled A, B, and C) have been incised several meters into the Pleistocene alluvial fan on the NE side of the fault. On the SW side of the fault, several small gullies are dextrally offset from these upstream channels. We proposed to excavate

across the gullies shown as boxes in Fig.1b. Last year, we started excavating the upstream trench and the youngest offset channel on the downstream side, both shown as yellow rectangles in Fig.1b.

During the past year, we continued the 3D excavation at this site, logging about 80 trench walls. Fig.2 shows the traces of the principal excavation walls in map view. In each trench cluster, the initial trench was parallel to and several meters from the fault. Subsequent faces were cut progressively closer to the fault, at increments of 50-60 cm, or 10-25cm if needed (for example, in the vicinity of the fault).

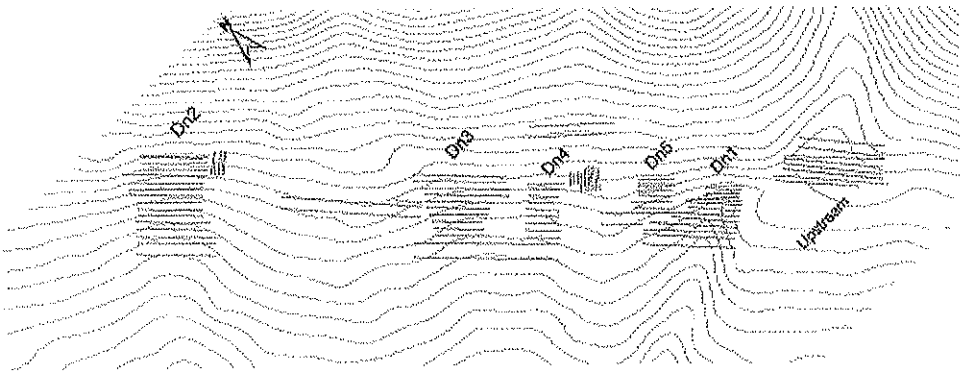

Fig.2 Traces of the principal excavation walls. The red lines indicate the locaion of the exposures shown in Fig.3a-f

Results:

Trench exposures

Fig. 3 shows the logs of representative cuts in each trench cluster, looking upstream, whose locations are shown as the red labeled lines on a map view in Fig.2. Fig.3a through e are those of the downstream channels. They are arranged from NW to SE, and by their geomorphic distance from the upstream channel. The distance indicates the relative ages of the channels, with the farther one being older. Fig.3f is the log on the upstream side.

Downstream

The downstream channels are 1-2m deep, mostly narrow, and covered with homogenous colluvium. Their thalwegs are generally well defined. The channels cut into massive bioturbated matrix-supported gravely sand and silt, with horizontal sandy and gravely lenses. A pedogenic carbonate horizon in this old deposits suggests that these deposits are several thousand years old, since in this region such concentrations of soil carbonate are only found in early Holocene or older deposits (Sieh and Jahns, 1984). The deposits within the channels are generally grayish, in sharp contrast with the surrounding whitish carbonate-coated Holocene alluvial fan deposits they cut into. The in-channel deposits consist of both poorly sorted gravely sand and silt, and well-sorted clast-supported channel sand and gravel beds.

Trench cluster dn2 lies about 55m NW of the upstream trench. Three channels were exposed in this trench cluster (Fig.3a). The middle channel, "Buwalda" is made up of

mostly massive loose clast-supported sand and gravels to pebbles. This channel contains the largest clasts among all the downstream channels. On the trench cut shown here, the channel is broad and deep, bounded by a fault on top. The channel deposit is 0.7 m thick on this cut. Yet, on other downstream cuts, the bedload is less than half the thickness. It is possible that the double thickness is due to faulting. There is a channel 3m NW of "Buwalda". A sample from a burn mark in the top part of this channel has 14C age of 2980+/-50 yrs. Given the slip rate of 35 mm/yr, this channel came from about 100 meters to the SE. The most probable candidate of its upstream half is the big channel "C" in Fig.1a. Channel "Wood" sits 2.5m to the SE of "Buwalda". It merges with "Buwalda" 2.5m downstream. The basal layer of bedload sand and gravels in "Wood" is continuous, and traceable.

Four channels were exposed in trench cluster dn3 (Fig.3b). "Wallace" is the leftmost channel. Most of its stratigraphy is destroyed by bioturbation. The remaining strata are two layers of sandy bedloads. One is at the base of the channel, the other one ~25cm above. The shallow channel 2m to the SE of "Wallace" is barely visible due to severe bioturbation. This channel merges with "Wallace" 5m downstream. Channel "Allen" is 1.5m further to the SE. It is deep and narrow, a series of bedloads are still visible near the bottom of the channel. "Weldon" lies SE of "Allen". The precise location of this channel is unclear on this wall due to severe bioturbation. On other downstream cuts, this channel is made up of the bedload of a cluster of 3-4 small channels, which merge with "Allen" 5m downstream from the fault.

In the three trench clusters that are closest to the upstream trench, we found three lone channels about 8 meters apart. Channel "Prentice" is the lone channel in trench cluster dn4 (Fig.3c). It is shallow and broad. Most of the in-channel strata are still well preserved. It has the distinctive domino-style stacking of three channels of sand and gravels. Fig. 3d shows the channel "Yule", a deep and narrow lone channel. It has a characteristic layer of upwardly fining sequence of horizontally bedded well-sorted sand and small gravels. Channel "Grant" is the youngest channel on the downstream side. It was offset 8-9 meters in 1857 earthquake. It is a double channel in this cut (Fig.3e). The main channel is the deep and narrow one on the left. The right one was previously inside the deep channel on downstream cuts. Channel "Grant" was bounded by fault on top.

Upstream

Upstream trench logs document a series of nested channels. There are 8 generations of channels that can be correlated with the downstream ones. The correlation is based on the relative ages, as well as the similarity in the shapes of channels and the initial filling of alluvium and colluvium in the channel. The relative ages of the channels is indicated by the cross-cutting relationships among the channels on the upstream side and on the downstream side by the amount of offset. The larger the offset the older the channel. We assigned names to all of the offset channels: each upstream channel bears the given name of a Caltech geologist who has studied the San Andreas fault; each downstream channel bears the surname.

Here is the brief description of the upstream channels from old to young. The oldest channel "John" is located near the base of our trench exposure. It is made up of a series of channel sand and gravels separated by homogeneous matrix-supported colluvium.

Unlike its downstream counterpart, this channel has a broad lens of silty fine sand, overlain by coarser sandy and gravely alluvium (colored in yellow in Fig.3f). The fines are suspended loads that settled from muddy water ponded upstream from the fault, after the earthquake brought a shutter ridge in front of the channel. The upstream channel was later buried further by coarser sandy gravel. Channel "Harry" was cut after "John" was filled up to the top of the shutter ridge. The earthquake that occurred after creation of Harry also brought a shutter ridge in front of the channel, which led to deposition of another lens of suspended load, on top of "Harry".

The next channel in this sequence is "Bob". Like the downstream channel "Wallace", it has two layers of bed-load sand and gravel near the bottom of the channel. Two suspended-load layers are associated with this channel. They are wide, and extend well outside the channel. These suggest that the event that occurred immediately after the cutting of channel "Bob Wallace" had a large vertical motion, with the downstream side moving up.

Three channels, "Clarence", "Ray" and "Carol", cluster on the upper NW part of the trench wall. "Ray" and "Clarence" are two older channels, cut by "Carol", and no obvious suspended load deposit was associated with them. Channel "Carol" has the similar domino-style stacking of three inset channels as the downstream channel "Prentice".

Like "Yule" of the downstream channel, channel "Doug" has the characteristic layer of well-sorted and horizontally bedded sand and gravels. Although "Doug" is a double channel on this cut, subsequent excavation shows that the side channel to the right merges with the deeper left channel 0.5m downstream. The youngest channel "Lisa" sits in the middle of the trench wall. A prominent suspended-load lens of well-sorted fine sand and silt plugs the channel. It is overlain by sand and gravel beds.

Traces of thalwegs of the channels

Our sequential excavation procedure has enabled us to keep track of the locations of channels along their course. It also has allowed us to detect the fault-related shift in channel course.

Our excavation shows that the upstream channels are straight, except channel "Harry" which diverges to the northwest, through the shallow declivity that subparallels the fault. They are offset by a secondary fault 1m upstream from the main fault (Fig.4). Younger channels, "Lisa", "Yule", "Prentice" and "Ray" were offset about 45 cm across this secondary fault; older channels were offset double that amount. It suggests that the secondary fault moved at least twice. The main fault zone is only about 0.5 meters wide.

On the downstream side, channels are separated by meters. They are also quite straight. The bases of four channels, "Buwalda", "Prentice", "Yule" and "Grant", runs into the fault at a high angle. Channel "Wood" is 3.5m to the SE of "Buwalda" at the fault and quickly merges with "Buwalda" 5-6 m downstream. It fits with the northwest divergence of the upstream channel "Harry". Channel "Allen" is straight except a gentle curvature about 1.5 to 4.5 m downstream from the fault. "Wallace" and "Weldon" join "Allen" from left and right respectively. "Wallace" diverges from the fault diagonally, trying to avoid the topographic high to the left. Also note that there is a channel flow almost parallel to fault before it joins "Prentice" 1.5 m downstream.

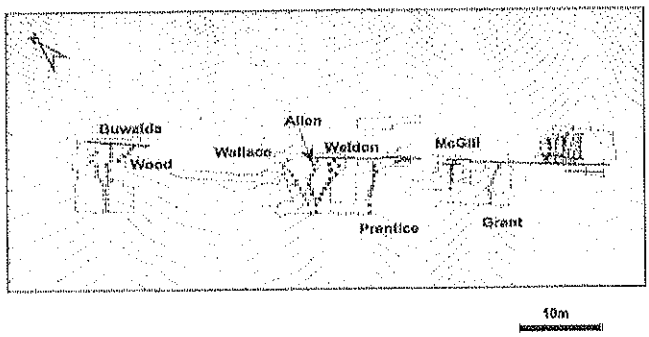

Fig.4 Traces of the thalwegs of the offset channels. The same channel on two sides of the fault is colored the same. For the convenience of references, each channel on the downstream side of the fault is named after a Caltech-graduate scientist who have worked on the San Andreas fault. The dark lines trending NE are fault traces exposed in the trenches. Most channels are straight and intercepted by the fault at a high angle.The main fault zone is narrow, about 1 meter wide, a secondary fault was found on the upstream side of the fault, and there is about 50-80 cm offset occurred on it.

Matching channels on two sides of the fault

The offset of the channels can be best visualized as shown in Fig.5. It is an imaginary view of the fault plane looking downstream. Red dots are the locations where the thalwegs of channels run into the fault. The shapes of the channels are also included for comparison. Upstream channels cluster on the left part of Fig.5, downstream channels spread on the right. Older channels were offset farther from the upstream channels as they experienced more earthquakes. The pairing of the same channel on two sides of the fault gives how much the channel has been offset since formed, both in horizontal and vertical.